Use of a high-entropy oxide as an oxygen carrier for chemical looping

Energy 298 (2024) 131307

Contents lists available at ScienceDirect

Energy

journal homepage: www.elsevier.com/locate/energy

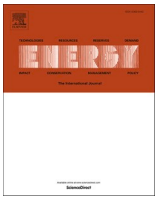

Use of a high-entropy oxide as an oxygen carrier for chemical looping

Iñaki Adánez-Rubio [a,*], María T. Izquierdo [a], Joakim Brorsson [b], Daofeng Mei [c], Tobias Mattisson [c], Juan Adánez [a]

[a] Instituto de Carboquímica (ICB-CSIC), Department of Energy & Environment, Miguel Luesma Castán, 4, Zaragoza, 50018, Spain
[b] Department of Physics, Division of Chemical Physics, Chalmers University of Technology, SE-412 96, Göteborg, Sweden
[c] Department of Space, Earth and Environment, Division of Energy Technology, Chalmers University of Technology, SE-412 96, Göteborg, Sweden

ARTICLE INFO

Handling editor: Krzysztof (K.J.) Ptasinski

Keywords:
High entropy oxygen carriers
Chemical looping
Oxygen uncoupling
Syngas

ABSTRACT

One mixed oxide with 5 cations in equimolar proportions in the sublattice, to fulfil high-entropy oxide (HEO) criteria, has been developed and investigated as oxygen carrier for chemical looping combustion processes. As far as we know, nobody has explored this class of material for chemical looping combustion. Material is prepared by direct mixing of five metal oxides (CuO, Mn_2O_3, Fe_2O_3, TiO_2, MgO), followed by calcination at 1000, 1100 and 1200 °C for 6 h in air. XRD characterization provides strong evidence that the synthesized oxygen carriers possess the hallmark properties of HEO, and SEM-EDX analysis shows an overall homogeneous metal distribution. Materials have one main cubic phase with the empirical formula $MnCuMgFeTiO_7$, dominating under all conditions. One of the key objectives of this study is achieved, reduce chemical stress during redox cycles. Oxygen transfer capability is investigated by thermogravimetric analysis and batch fluidized bed reactor experiments for different fuels and atmospheres. Mass-based oxygen transport capacities for lattice oxygen and oxygen uncoupling are around 5.5 wt% and 1.1 wt%, respectively. This work opens up a new dimension for the future preparation of oxygen carriers for chemical looping processes, since the vast compositional space of HEO provides opportunities to tune both chemical and physical characteristics.

1. Introduction

CO_2 capture and storage (CCS) systems are widely regarded as effective, albeit temporary, options for reducing anthropogenic emissions [1]. Specifically, these allow CO_2 to be captured from energy-related sources before being transported and stored at a suitable storage site, preventing it from entering the atmosphere. Chemical looping (CL) processes can be used for a variety of efficient fuel conversion processes [2,3]. These include chemical looping gasification (CLG) and chemical looping combustion (CLC), which are suitable for low-cost CO_2 capture [1]. In a CLC process, metal oxides, also referred to as oxygen carriers (OCs), are used to transport oxygen between the air reactor and the fuel reactor, thereby preventing direct contact between the air and fuel. Consequently, only CO_2 and H_2O form in the fuel reactor, given that combustion is complete. In the air reactor, the used OC is regenerated with O_2 in preparation for the next cycle, which means that the only outlet gases are N_2 and unreacted O_2.

A substantial number of OCs have been tested over the past two decades, ranging from simple mono-metallic oxides to complex and multi-component oxides, such as perovskites [2–7]. High-entropy oxides (HEOs) form a relatively new class of materials that have been intensively studied for diverse energy applications [8], including catalysis [9–16] and energy storage [17–21]. While no precise definition exists for high-entropy materials (HEMs), a consensus has been reached regarding some of their key characteristics. Specifically, a HEM should consist of a single crystalline phase in which the constituent elements are randomly distributed on all length scales. Although the lower limit on the configurational entropy is still under debate, a common criterion is that the value should be greater than 1.5R [22], where R is the gas constant. While this rule originally stems from a naïve estimate of the configurational entropy of an alloy with five distinct elements, for which $S_{conf} = 1.61R$ [8,22,23], experiments have verified that certain functional properties are enhanced above this limit.

While an equimolar mixture will give the highest configurational entropy, slight deviations from such a composition could potentially enhance key properties for a given application, which would therefore provide significant possibilities for optimization. As long as the $S_{conf} \geq 1.5R$ criterion is satisfied, the phase should be stabilized and thus

* Corresponding author.
E-mail address: iadanez@icb.csic.es (I. Adánez-Rubio).

https://doi.org/10.1016/j.energy.2024.131307
Received 15 December 2023; Received in revised form 4 April 2024; Accepted 12 April 2024
Available online 17 April 2024

less prone to decomposition, particularly at high temperatures. Although the exploration of OC materials in recent decades has resulted in a large number of possible compositions, there are some compelling reasons why HEOs could also be of great interest also CL. In addition to opening up a vast number of new compositions, the use of HEOs presents a possible solution to the loss of stability of OC particles due to the chemical stress induced by the reduction-oxidation (redox) cycles [24–30]. Furthermore, theoretical and experimental research suggest that there could be other benefits. Notably, there is evidence of the stabilization of oxygen vacancies [31], increased oxygen mobility [32], and sluggish metal atom diffusion, as well as improved mechanical properties [8]. Consequently, the use of HEOs could potentially solve some of the key issues related to OCs for CL processes, i.e., by enhancing the capacity and rate of oxygen release, as well as the resistance to attrition, fragmentation, and decomposition. As of yet, such materials have not been studied as OCs for CL combustion processes. Recently it has been published a study of the use of a HEO as oxygen carrier for the production of H_2 by chemical looping reforming coupled with water splitting (CLR-WS) in a fixed bed reactor [33]. They obtained good results in terms of H_2 generation using toluene as a model fuel. However, they found that the main phase changed after the reduction step, from HEO to High entropy Alloy (HEA) [33].

For the purpose of exploiting the possible advantages previously described, a mixed oxide was prepared according to the principles of HEMs with the intention of testing its use as an OC. Pure oxides of Cu, Mn, Fe, Ti and Mg were used in the synthesis. The selection was based on previous research into mixed metal oxides for CLC and Chemical Looping with Oxygen Uncoupling (CLOU) [34,35]. Three of the metals form oxides with redox properties. Specifically, those based on Cu and Mn are able to release O_2 at high temperature for CLOU, or lattice oxygen for CLC [34,35]. Oxides of Fe are also well-known OCs, although they do not typically possess properties that enable the release of oxygen to the gas phase at relevant temperatures. The prepared materials were characterized by X-ray diffraction (XRD), scanning electron microscopy (SEM), and energy dispersive X-ray spectroscopy (EDX). Properties related to the release of gaseous O_2 for CLOU and lattice oxygen for CLC in redox cycles were investigated using a thermogravimetric analyzer (TGA) and a batch fluidized bed reactor (BFBR) for the purpose of analyzing the suitability of the materials as OCs.

2. Experimental section/methods

2.1. Oxygen carrier

In order to prepare the high-entropy oxygen carrier (HEOC) material, five powdered metal oxides (CuO [Merk, ≥99%], TiO_2 [Sigma Aldrich, ≥99.8%], Fe_2O_3 [Fisher Scientific, ≥99.8%], MgO [Sigma Aldrich, ≥97%], Mn_3O_4 [Sigma Aldrich, ≥97%]) were mixed in equimolar fractions. The mixture was ground in a ball mill (alumina jar with zirconia balls) overnight before being calcined in a muffle furnace in air for 6 h at 1000, 1100, or 1200 °C, and then allowed to cool freely inside the furnace. The heating ramp for calcination was as follows: 20 °C/min from room temperature to 800 °C, 5 °C/min from 800 °C to the set calcination temperature, followed by 6 h of calcination at the desired temperature. The HEOCs were finally milled and sieved to obtain particles with a size of 100–250 μm.

A Shimpo FGN-5 digital force gauge apparatus was used to determine the crushing strength which was then used as the force required to break a particle. The values for all the HEOC materials, each averaged over at least twenty measurements on randomly chosen particles within the desired range of 100–250 μm, were found to be higher than 2 N and did not depend on the calcination temperature. Note that a crushing strength higher than 1 N is considered acceptable for use in CL systems [36].

XRD was used to identify the crystalline solid phases. The corresponding diffractograms were collected by a Bruker D8 Advance X-ray powder diffractometer, equipped with an X-ray source in the form a Cu anode working at 40 kV and 40 mA, and an energy-dispersive one-dimensional detector. In all cases, the diffraction pattern was recorded over a 2θ range of 10°–80° with a step of 0.019°. The phases in the HEOCs were identified using DIFFRAC. EVA software, which supports a reference pattern database derived from the Crystallography Open Database (COD) and Powder Diffraction File (PDF).

Microstructure was examined via SEM-EDX analysis using a JEOL JSM-7800F Prime instrument. To expose the cross-sections, some of the samples were dispersed in epoxy resin, modulated, cut, and polished before SEM−EDX characterization.

In order to establish the metal distribution within the particles, micrographs were analyzed using the positive matrix factorization (PMF) method [37], also known as nonnegative matrix factorization (NMF) [38]. This is a multivariate factor analysis technique that has been successfully used in CLC applications [39]. The function of the PMF is to identify factors that can describe common features between datasets. In the present work, the PMF method was applied to the elemental maps obtained from the SEM-EDX analysis through the use of an open-source EPA PMF program [40]. In addition, the correlation between each two elements were quantified through Pearson correlation coefficient which was calculated with a MATLAB code developed in previous work [39]. This means that the clustering results show the correlations between the elements and their spatial distributions. More information on this technique can be found elsewhere [39].

2.2. Experimental methods

In order to assess whether the synthesized materials could function as HEOCs, experiments were conducted to determine their oxygen transfer capacity, as well as their ability to release gaseous oxygen, which has been found to be highly beneficial for the fuel conversion process.

2.2.1. Thermogravimetric analyzer

The reactivity of the HEOCs was tested in a TGA through multiple redox cycles, either with H_2 and CH_4 as fuels, or with N_2 to determine their oxygen uncoupling capability, while air was used to analyze the oxidation reaction. Details regarding the TGA (CI Electronics) has been described elsewhere by Adánez et al. [41].

Data evaluation: OC conversion was calculated as follows, using reactivity data obtained from the redox cycles in the TGA:

Reduction:

$$X_{Red} = \frac{m_{Ox} - m}{m_{Ox} - m_{Red}} \tag{1}$$

Oxidation:

$$X_{Ox} = 1 - \frac{m_{Ox} - m}{m_{Ox} - m_{Red}} \tag{2}$$

here m is the sample mass at each time; m_{Ox} the mass of the fully oxidized sample; and m_{Red} the mass after complete reduction. The rate index (RI) was calculated as:

$$RI = 100 \cdot 60 \cdot \left(\frac{d\omega}{dt}\right)_{norm} = 100 \cdot 60 \cdot R_{OC} \cdot \left(\frac{dX_i}{dt}\right)_{norm} \tag{3}$$

here,

$$\omega = \frac{m}{m_{Ox}} = 1 - R_{OC}(X_{Ox} - 1) = 1 - R_{OC}X_{Ox} \tag{4}$$

is the mass-based conversion and X_i is the conversion for reduction or oxidation. The normalized reactivity is defined as:

$$\left(\frac{dX_i}{dt}\right)_{norm} = \frac{P_{ref}}{P_{TGA}}\left(\frac{dX_i}{dt}\right) \tag{5}$$

where P_{ref} is the reference partial pressure of the fuel gas (0.15 atm), and P_{TGA} is the partial pressure of the gas used in the TGA experiments.

2.2.2. Batch fluidized bed reactor

Experiments for analyzing CLOU behavior were carried out in a quartz BFBR with a height of 870 mm high and width of 22 mm. Fig. 1 shows the experimental setup scheme used in the present work, which has been described in detail elsewhere [11,42]. The exit gas stream from the reactor was led into a condenser to remove the water produced during H_2 combustion. The composition of the dry gas was determined by a Rosemount NGA-2000 analyzer, which measured the concentration of O_2 through a paramagnetic channel; CO_2, CO, and CH_4 through infrared channels; and H_2 through thermal conductivity.

Experimental procedure: For each batch of HEOC particles, 15 g of particles were introduced into the BFBR, oxygen release and regeneration experiments were carried out at 850, 900, and 950 °C under CLOU conditions (N_2 flow stream of 850 ml/min) followed by reactivity experiments with synthesis gas (50 vol% H_2 and 50 vol% CO, with a flow stream of 450 ml/min) at 950 °C. After repeating the previously described experiments, the samples were removed from the reactor before being checked for signs of bed agglomeration with naked eyes and SEM. In all cases, oxidation took place in a stream with 11 vol% of O_2, N_2 for balance, and a flow rate of 850 ml/min. Each HEOC was, consequently, analyzed for a duration of approximately 10 h of high-temperature fluidization. More details regarding the BFBR experiments can be found in section 1 of the Supplementary Material (SI).

Data evaluation: Equation (6) was utilized to calculate the reduction conversion X_{red} as a function of time from the measured concentrations of different gaseous species during the reduction period:

$$X_{red} = \frac{1}{R_{OC}} \int_{t_0}^{t_1} \frac{\dot{n}_{out} M_O}{m_{ox}} \left(2y_{CO_2} + y_{CO} + 2y_{O_2} - y_{H_2}\right) dt \quad (6)$$

where X_{red} is the instantaneous mass-based conversion at time t_1, $\dot{n}_{out}$ the molar flow rate of dry gas at the reactor outlet as measured by the analyzer, and M_O the molar mass of oxygen, while t_0 and t_1 represent the initial and final time of measurement.

The reactivity of a given OC is quantified in terms of CO_2 yield, γ_{CO_2}, and is defined as the fraction of fully oxidized fuel divided by the carbon- and hydrogen-containing gases in the outlet stream:

$$\gamma_{CO_2} = \frac{y_{CO_2}}{y_{CO_2} + y_{CO}} \quad (7)$$

The H_2 conversion, X_{H_2}, is defined as:

$$X_{H_2} = 1 - \frac{y_{H_2,e}}{y_{H_2,i}} \quad (8)$$

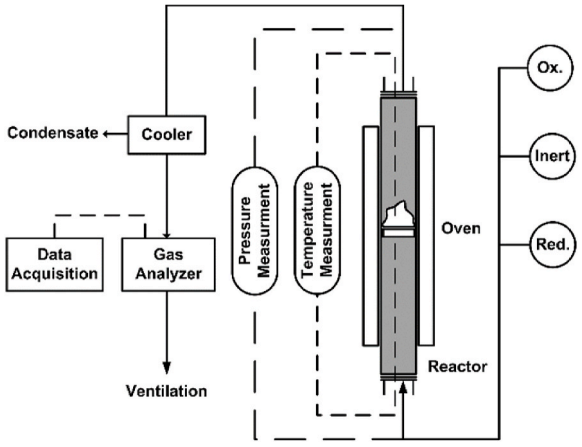

Fig. 1. Diagram of the experimental setup used in this work [11,42].

here $y_{i,e}$ denotes the concentrations (vol%) obtained from the gas analyzer in the exit stream, and $y_{i,i}$ the concentrations (vol%) of the respective gases fed to the reactor.

3. Results

3.1. HEOC characterization

The prepared HEOCs were characterized in order to verify whether they possessed the hallmark properties of HEOs, and their main properties are listed in Table 1. Based on comparisons with previous works [2,3], their OC characteristics were deemed to be acceptable.

Fig. 2 shows the XRD patterns of fresh particles after calcination at different temperatures in air. Evidently, there are no significant differences between the three diffractograms since all indicate the presence of a major cubic phase, together with a contribution from a minor rhombohedral phase. It should be noted that no reference for a single crystal phase that contains all five of the metallic elements used in the synthesis of the HEOCs could be found in the Inorganic Crystal Structure Database (ICSD). However, multiple entries from the Powder Diffraction File (PDF) database could be fitted to the peaks assigned to cubic structures (e.g., PDF 89–2807 $Mn_{0.43}Fe_{2.57}O_4$, PDF 75–1373 $Fe_{2.75}Ti_{0.25}O_4$, PDF 73–2314 $CuFe_5O_8$, PDF 74–2072 $Cu_{0.5}Mn_{0.5}Fe_2O_4$), while the peaks assigned to rhombohedral structures are compatible with PDF 06–0494 $MgTiO_3$. This is in agreement with an earlier work on perovskites in which different polymorphic phases with rhombohedral or cubic structures were obtained depending on the cooling rate applied during the synthesis process [43]. According to Aamalid et al. [22], the presence of secondary phases could be related both to the cooling rate and the preparation method. In particular, solid-state synthesis, used in the present study, has in some cases been associated with a higher degree of elemental segregation.

3.2. HEOC CLC/CLOU reactivity in TGA and batch fluidized bed reactor

3.2.1. TGA reactivity

According to Fig. 3 (a), which shows the reduction conversion with H_2 (15 vol% H_2+20 vol% H_2O) at 800 °C as a function of time, reactivity was very high and showed no significant variation between the different calcination temperatures. As indicated in Table 1, the same applies to the oxygen transport capacity associated with the lattice oxygen supply (R_{OCL}), and a value of around 5.5 wt% was obtained in all three cases.

To assess the release of gaseous O_2, oxygen release capability, $R_{OC,CLOU}$, was measured by reduction in a TGA at 950 °C in N_2. Fig. 3 (b) shows that CLOU reduction reactivity was low, even though it increased slightly with the calcination temperature. Although $R_{0C,CLOU}$ was limited to 1.2–1.1 % and given that there is room to improve the oxygen transport capacity for combustion processes, these materials have interesting properties and can be used in other processes, for example, for a controlled supply of O_2 in other oxidation processes such as dehydrogenations [11]. Table 2 shows a comparison of the oxygen

Table 1
Properties of the fresh HEOC calcined at different temperatures in air.

	HEOC_1000		HEOC_1100		HEOC_1200	
	Fresh	Used	Fresh	Used	Fresh	Used
Oxygen transport, R_{OCL} (wt %)	5.5	5.6	5.6	5.8	5.4	5.6
Oxygen transport, $R_{OC,CLOU}$ (wt%)	1.2	1.2	1.1	1.2	1.1	1.2
Crushing strength (N)	2.3	2.0	2.2	2.1	2.3	1.9
Bulk density of particles (kg/m^3)	3450	3420	3500	3490	3420	3400
Specific surface area, BET (m^2/g)	<0.5	<0.5	<0.5	<0.5	<0.5	<0.5

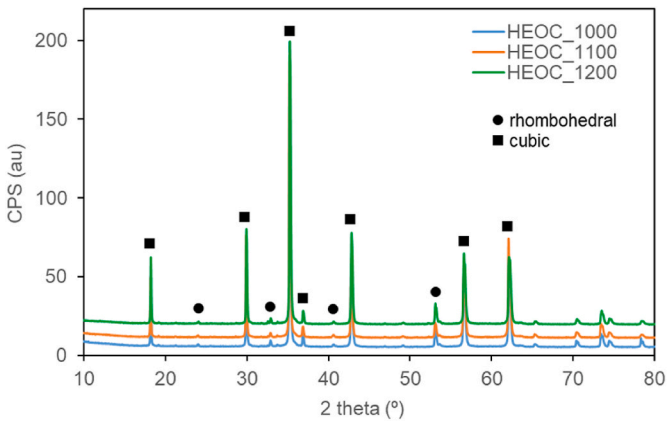

Fig. 2. (a) XRD profile of HEOC particles calcined at different temperatures in air.

transport capacity for oxygen carriers based on simple oxides and oxides containing 2, 3 and 4 metallic elements, as representative of low-medium entropy oxides. It is clear that, the oxygen transport capacities and reactivities of the HEOCs are of the order of magnitude as oxygen carriers previously tested in continuous units.

As can be seen from Fig. S1, all the O_2 transferred in the lattice oxygen and oxygen uncoupling reactions can be regenerated, which indicates that the oxidation reactions were complete. A similar behavior was observed when using CH_4 as fuel, as shown in Fig. S2. OC conversion was completed in both redox reactions, and reactivity was maintained across the redox cycles.

The RI for the different reactions was determined and compared with values reported for different OCs used in CLC [3,24,46] and CLOU [4,45,52,53] processes. According to Table S1, the HEOCs have comparable rates for both reduction and oxidation reactions.

3.2.2. *Batch fluidized bed experiments*

BFBR can be seen as a complementary technique for determining reactivity and CLOU properties. It also provides information on behavior under more realistic conditions, i.e., redox reactions during fluidization. In total, the materials were subjected to 30 h of operation, which included cycles that either mimicked CLOU conditions or involved burning syngas via CLC.

The time evolutions for O_2 release and OC conversion are plotted in Fig. 3 (c) for different operating temperatures when fresh material was used. The released oxygen concentration follows a profile that is typical for mixed oxides, since it increases with temperature and displays a direct correspondence with OC conversion [54–59]. The values were almost always lower than the equilibrium concentrations for the active redox pairs CuO/Cu_2O and Mn_2O_3/Mn_3O_4, except at 850 °C, where the HEOC released more O_2 than previous Cu-based and Cu–Mn mixed oxides CLOU OCs (see Fig. S5). As expected, reduction conversion increased with operating temperature.

The same experiments were conducted using samples taken after the syngas combustion. The activation of the particles is clearly indicated by the slightly higher oxygen concentration and the significant increase in the reduction conversion visible in Fig. 3 (d), which shows a comparison

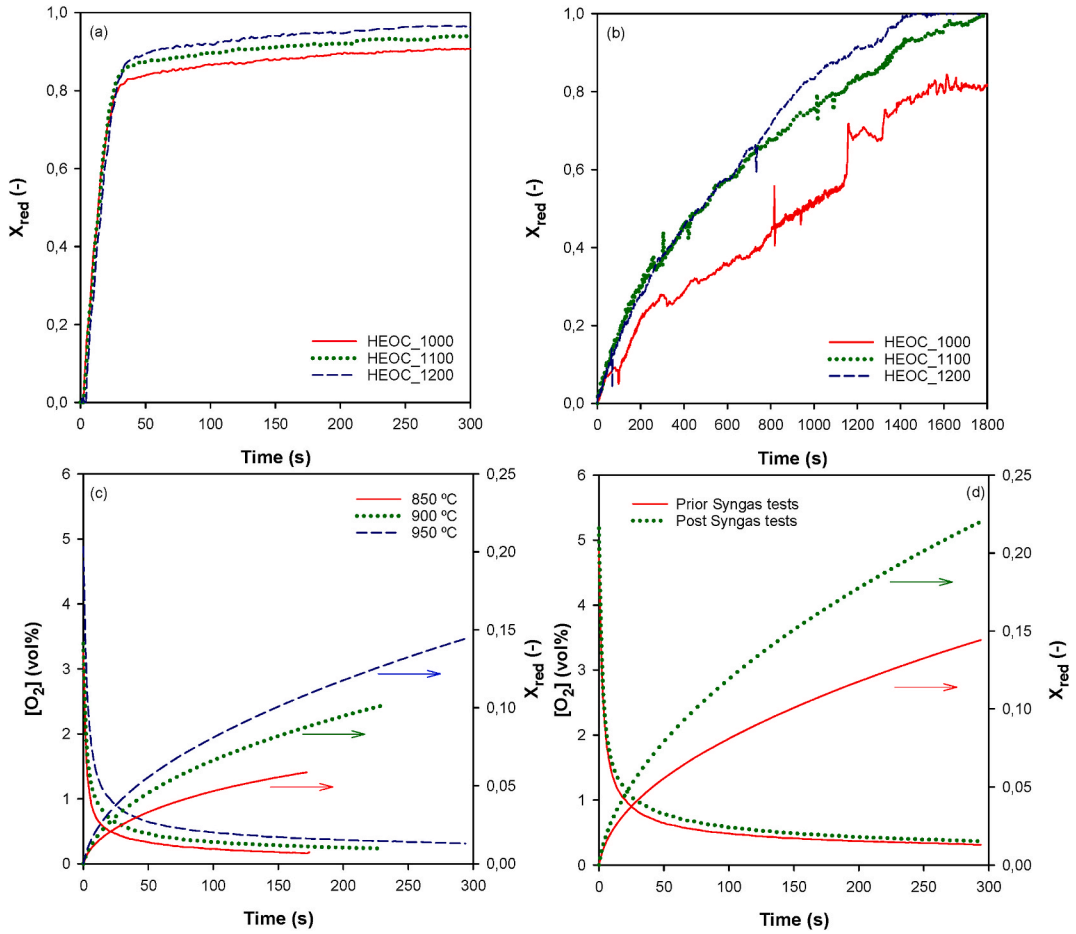

Fig. 3. The reactivity of prepared materials when (a) reduced with H_2 at 800 °C and (b) in an oxygen uncoupling reaction at 950 °C, measured in a TGA, in addition to O_2 generation and OC reduction conversion (c) at different temperatures and (d) before and after syngas combustion at 950 °C obtained from BFBR experiments for fresh HEOC_1100.

Table 2
Comparison of the oxygen transport capacity for oxygen carriers based on simple oxides and oxides containing 2, 3 and 4 metallic elements, as representative of low-medium entropy oxides.

Number of metallic elements	Active phase/support	Oxygen transport, R_{OCL} (wt%)	Oxygen transport, $R_{OC,CLOU}$ (wt%)	Entropy	Reference
1	Hematite	2.4	–	Low	[2]
	Mn-ore	5.1	2.2	Low	[44]
	Cu/Al_2O_3	3	1.5	Low	[2]
	$Fe–Al_2O_3$	5.1	–	Low	[2]
	$Cu/MgAl_2O_4$	12	6	Low	[45]
2	Ilmenite	4	–	Low	[46]
	Cu–Mn	8	4	Low	[29,34]
	$CaMnO_{3-\delta}$	0.9	–	Low	[47]
3	$CaMn_{0.875}Ti_{0.125}O_3$	9	1.2	Low-Medium	[48]
	$CaMn_{0.9}Mg_{0.1}O_{3-\delta}$	10.1	1.5	Low-Medium	[49]
	Cu30MnFe_mag	4	2	Low-Medium	[34,35]
	Cu30MnFekao7.5	4.6	2.3	Low-Medium	[50]
4	$CaxLa_{1-x}Mn_{1-y}M_yO_{3-\delta}$	–	0.37–0.76	Medium	[51]
	$CaMn_{0.775}Ti_{0.125}Mg_{0.1}O_{2.9-\delta}$	9.1	1.6	Medium	[51]
5	$MnCuFeMgTiO_7$	5.4	1.1	High	Present Work

between the results obtained before and after the syngas tests at 950 °C. This fact was corroborated by the TGA analysis, since an increase of the ROC,CLOU from 1.1 to 1.2 wt% and the ROCL from 5.6 to 5.8 wt% was observed for HEOC_1100, see Table 1, while still maintinating1 and maintaining the reactivity, see Fig. S4. Moreover, the crushing strength only shows a slight decrease for HEOC_1000 compared to HEOC_1100 while HEOC_1200 is more stable. Finally, the oxygen carriers calcined at different temperatures can be fully regenerated in both the batched reactor and TGA tests.

3.3. Characterization of oxygen carrier particles

3.3.1. XRD characterization

XRD diffractograms for the HEOCs in the oxidized state were collected after the BFBR experiments. As can be seen in Fig. 4 (a), the main change between the patterns of the fresh and used samples is the increase in the intensity of the rhombohedral phase in the latter.

A decrease in the metallic elements involved in the cubic structure could lead to a contraction, while reduced oxygen content can weaken the lattice and expand the cell. This has been observed in a number of Cu-containing perovskites and Brownmillerite type structures, which leads to the coexistence of cubic and rhombohedral domains [60]. Nevertheless, a high number of cationic vacancies can make the phases unstable and, depending on the metals ratio, cause a segregation to occur.

A detailed high-angle reflection is included in Fig. 4 (a), which gives a qualitative idea as to the changes after the BFBR experiments. The presence of two partially overlapping peaks for the fresh sample suggests the presence of a pair of cubic phases with different cell parameters.

However, after use in the BFBR, the shapes are considered to have changed since the lower (higher) angle peak decreases (increases) in height, suggesting a partial transformation of the corresponding phases. According to Fig. 4 (a), the overall reduction in the contribution from cubic phases is, moreover, linked to an increase in the rhombohedral phase content. This could be a consequence of the temperature changes during the redox reactions in the BFBR and the following cooling, as explained in the section concerning characterization of the fresh HEOCs.

3.3.1.1. Effect of redox processes on crystalline HEOC phases. Fig. 4 (b) shows XRD profiles collected for the reacted particles after the TGA tests, following reduction via oxygen uncoupling, as well as reoxidation. Though a new phase appears in the sample reduced by CLOU, it disappears after reoxidation.

Accordingly, the main differences are found in the reduced sample, in the form of new peaks that could be fitted with other rhombohedral phases (PDF 83–1284 Cu_3TiO_4 and PDF 750519 $FeTiO_3$). The emergence of deficient phases could be due to oxygen vacancy-induced rhombohedral transformations from the cubic phases [60]. This could explain the limited oxygen release capability in the TGA experiments reported in section 3.1. In addition, if Cu is found in the new phase (PDF 83–1284 Cu_3TiO_4), this could have an impact on the CLOU performance.

XRD patterns were collected and evaluated for partially reduced samples, i.e., with H_2 for 30 s to reach 50% of X_{red}, as well as after full reduction in the TGA. As can be seen from Fig. 4 (c), the corresponding XRD patterns feature new peaks that could be fitted with reduced copper species PDF 04–0836 Cu and PDF 39–0246 $CuFeO_2$. Still, all the main peaks present in the fresh sample are also found in the reduced samples, except for those that correspond to ilmenite, which decreased after 50% reduction and disappeared after 100% reduction. It should be noted that the reduced copper phases vanish in favor of the cubic phases after re-oxidation, resulting in a crystal state similar to that of the fresh sample. This fact is in agreement with the results obtained in the TGA measurements of HEOC reactivity, which is stable across multiple cycles.

3.3.2. SEM-EDX

The shape of the particles as well as their metal distribution were analyzed using SEM-EDX. It is apparent that the particles do not show any structural modifications after use in the BFBR (see Fig. S6). As can be seen from the SEM-EDX mappings in Fig. 5, a homogeneous distribution of the five elements can generally be observed in the interior of both a fresh and an oxidized particle, taken from the BFBR after 30 h of operation and a cool-down from 950 °C at a rate of 90 °C/min.

In SEM images Fig. 5 (a) and (g), dark areas can be observed, which occur more frequently and are larger in the fresh particle. The EDX mappings in Fig. 5 (b) and (h) show that these subdomains are enriched in Mg, while the other metallic elements are practically undetectable. A plausible explanation could be the different cool-down rates experienced by the fresh particles after calcination (slow cool-down) and the used particles in the BFBR (fast cool-down at a rate of 90 °C/min). Another reason could be the charge balance since, unlike the other elements, Mg cannot have multiple oxidation numbers. In particular, one should consider the fact that there should be a semi-local charge balance in the structure, which would be easier to accommodate if all the metallic elements within a certain volume are flexible with regards to their valence. The fact that Mg does not even become completely dissolved in the fully oxidized HEOC indicates that the charge balance would not be maintained if all the Mg atoms were to be incorporated into the main cubic phase. It is therefore quite reasonable that more Mg is “lost” as the amount of oxygen decreases.

However, most of the particles do not show this Mg segregation at microscale, as can be seen in Fig. S6, and the number of particles with theses clusters are reduced after their use in the BFBR. Therefore, in accordance with Aamalid et al. [22], given the presence of this

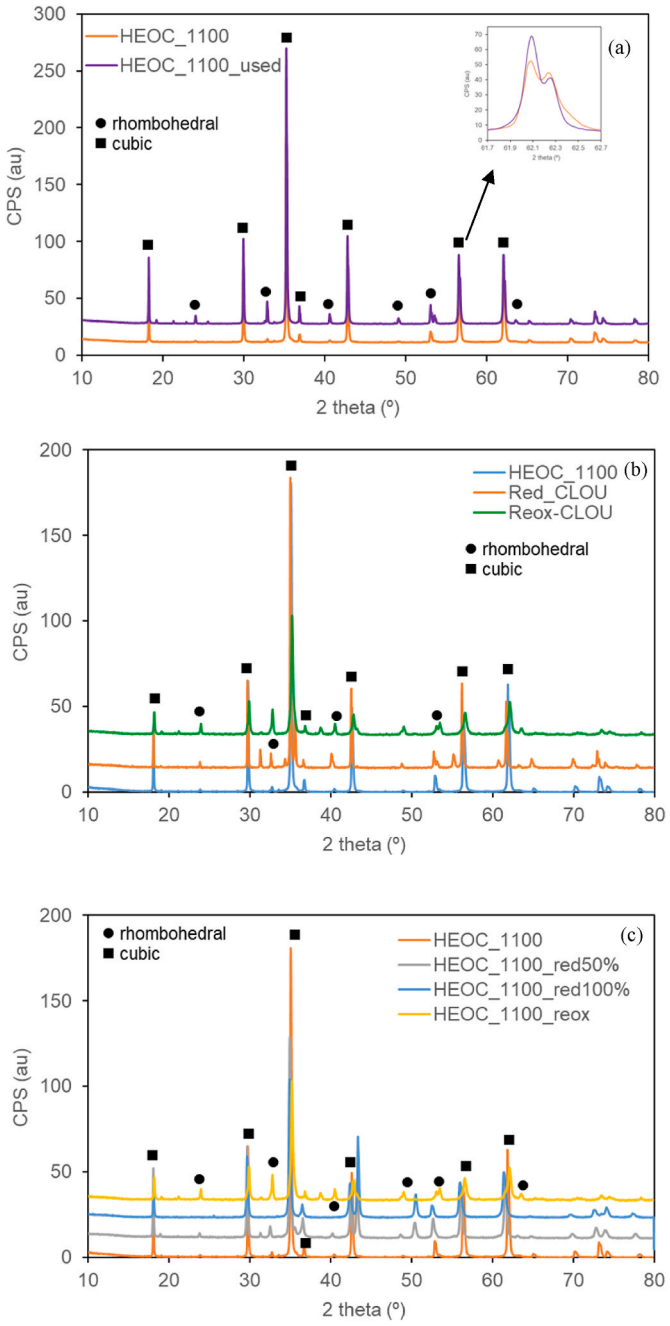

Fig. 4. XRD patterns showing comparisons between fresh HEOC_1100 and samples collected after (a) the BFBR and TGA experiments, including oxidation in air, under (b) CLOU and (c) CLC (15 vol% H_2 + 20 vol% H_2O) conditions.

clustering, its origin, and the scale with which it can be observed, we can include the OC material prepared in the present work under the umbrella of HEO, and are, thus, classified as HEOC material.

To gain a better understanding of the chemical composition of the particles, point EDX analyses were performed in the main part of their interior and Mg-enriched subdomains, as well as the transition zones (see Fig. S7). The results, compiled in Table S3, indicate that there is an even distribution of Cu, Mn, Fe, Ti, and Mg (Cu:Mn:Fe:Ti:Mg = 1:1:1:1:1) in the main region. The corresponding empirical formula, $MnCuMgFeTiO_7$, is consistent with the theoretical formula, $MnCuMgFeTiO_{6.8}$, which is obtained by combining stoichiometric amounts of CuO, Fe_2O_3, Mn_3O_4, TiO_2, and MgO. The Mg-enriched subdomains mostly consist of oxygen and Mg (33.3–33.8 at%), together with small amounts of Cu (around 3 at%) and Mn (around 2 at%). Specifically, this would correspond to the empirical formula $MnCuMg_{12}O_{22}$.

3.3.3. *Positive matrix factorization analysis*

The Pearson correlation coefficients between the elements in the HEOC particles were obtained from statistical analysis and are presented in Table 3. Obviously, pairs consisting of only a single element are linearly associated as the resulting coefficients equal 1. The coefficients involving combinations of different elements, meanwhile, are always lower than 1, meaning that the elements are not linearly dependent and could possibly have a nonlinear relationship. Since all such coefficients are in a narrow range of 0.54–0.70, this can be seen as a further indication that the metallic elements are all evenly distributed within the material.

PMF analysis was performed on the EDX mappings of both the fresh and used HEOC samples. According to a factor selection study using several factor numbers, the use of six factors is found the most appropriate. In particular, the use of six factors for the PMF analysis gives the best match between corresponding “base” and “boot” values in the EPA PMF program, which is a key criterion for proper factor selection.

Fig. 6 shows the species and factor profile from PMF analysis for used HEOC_1000. The species (factor) profile gives the percentage of each factor (element) in every element (factor). In particular, Ti is found to be mainly associated with factor 4, O with factor 3, Mn with factor 6, Mg with factor 5, Fe with factor 1, and Cu with factor 2, and vice versa. The fact that all six elements can be relatively well separated into six distinct factors should be regarded as additional evidence of an even elemental distribution. Furthermore, the reconstructed EDX images, which are shown in Fig. 7, are found to be consistent with the originals.

4. Discussion

One of the objectives behind the preparation HEOCs was to minimize chemical stress during redox cycles, and thereby the structural changes caused by both reduction and oxidation reactions. Encouragingly, the main phase was retained throughout the redox cycles in a TGA for both complete and 50% reduction with H_2. While some minor phases disappeared in the fully reduced sample, they were recovered after oxidation. Although similar results were observed for the oxidized samples taken after the syngas redox cycles in the BFBR, they showed small crystalline phase changes. This suggests reduced chemical stress across the redox cycles, which warrants further investigation in order to optimize the material synthesis and open new possibilities for investigating combinations of metal oxides for use as HEOCs. At the same time, the BFBR tests did not indicate any major attrition or reactivity loss, in spite of the slight tendency for segregation. Given the moderate reactivity of the HEOC material produced in this study, it could be used for modulated oxygen supply in processes other than CLC and CLOU, such as selective oxidation and oxidative dehydrogenation reactions of hydrocarbons [10,11].

The fact that a minimum of five cations are needed in order to achieve a sufficiently high configurational entropy means that the compositional space for HEOs is enormous. It can therefore be speculated that more optimized systems can be found that are better suited for specific CL applications. As an example, there are 4242 ways of combining five of the metals that are either currently found in OCs (Co, Cr, Cu, Fe, Mn, Ni, and V), provided that there must be at least one, or materials that can act as supports (Al, Ba, Ca, Ce, La, Mg, Sr, Ti, and Zr). Nevertheless, some of these combinations will likely not form a single phase. It is, however, possible to tweak the ratios between the elements for the purpose of, for instance, increasing oxygen transfer capacity and, hence, usability as an OC. HEOCs could also be selected based on the crystal symmetry, given that perovskite, spinel, rock salt, pyrochlore, magnetoplumbite, bixbyite, garnet, monoclinic, rutile, and even lamellar structures have been reported [32].

As far as we know, this material is the first that fulfills the main

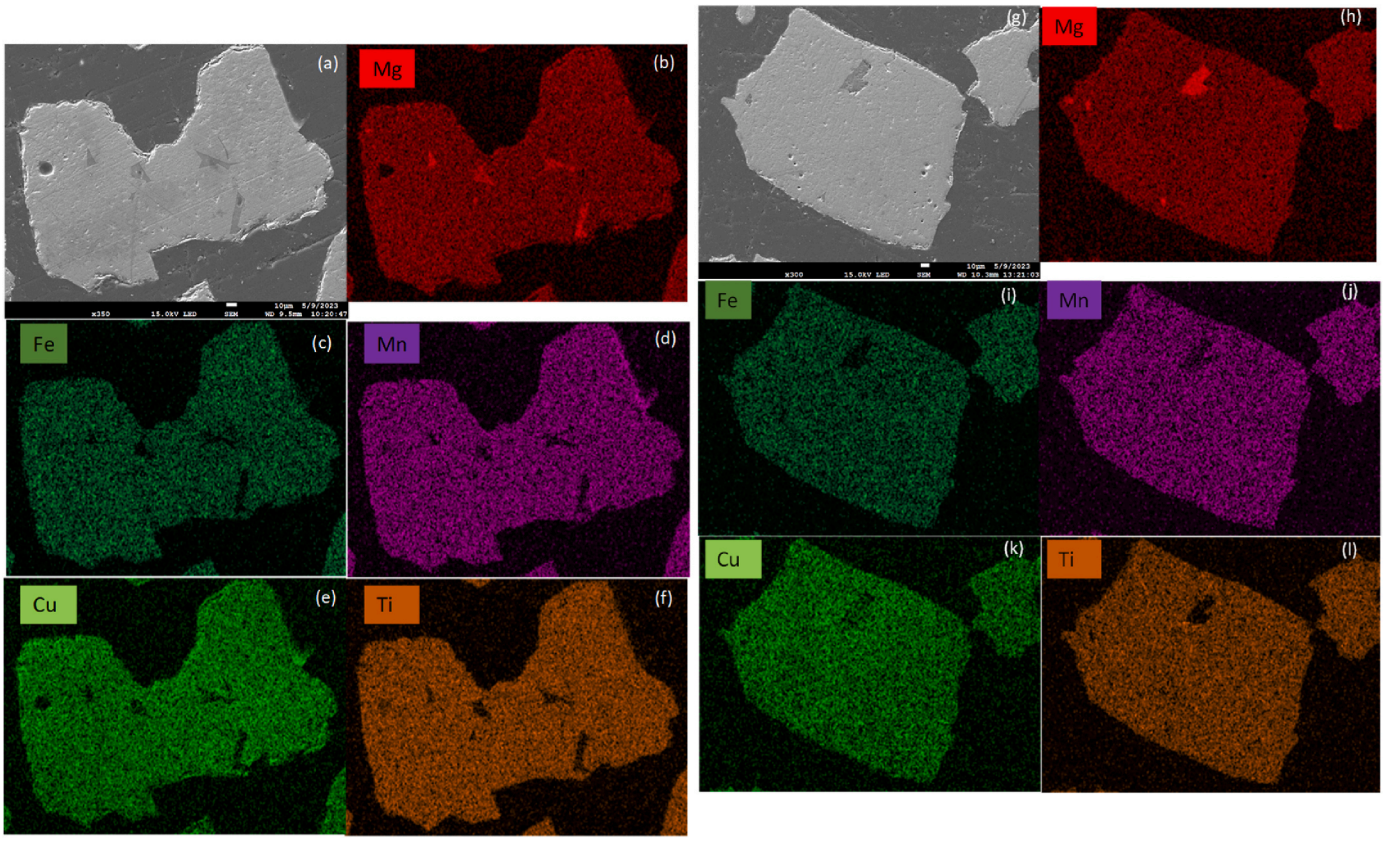

Fig. 5. SEM-EDX mapping of different elements present in the inner part of fresh (a–f) and used (g–l) HEOC_1100 particles: (a,g) SEM image; (b,h) Mg-mapping; (c,i) Fe-mapping; (d.j) Mn-mapping; (e,k) Cu-mapping; (f,l) Ti-mapping.

Table 3
Coefficients of all the elements based on a statistical analysis using EDX mapping (x75) of fresh HEOC_1100.

	Cu	Fe	Mg	Mn	O	Ti
Cu	1					
Fe	0.54	1				
Mg	0.61	0.57	1			
Mn	0.57	0.54	0.62	1		
O	0.59	0.57	0.67	0.61	1	
Ti	0.65	0.60	0.70	0.63	0.68	1

structural criteria for HEOs and is suitable for CLC reactions. However, further investigations are needed to measure its performance in a continuous unit to demonstrate that the attrition losses are reduced, thereby increasing the lifetime of the oxygen carrier.

5. Conclusion

Five metal oxides (CuO, Mn_2O_3, Fe_2O_3, TiO_2, MgO) were mixed in equimolar proportions and calcined to produce HEOCs. XRD analysis of the fresh particles suggest the presence of one main cubic crystalline phase together with a minor rhombohedral phase in both the reduced and oxidized states.

SEM-EDX analysis showed that the metallic elements are, on the whole, evenly distributed within the particles and suggests that the material can be represented by the empirical formula $MnCuMgFeTiO_7$. Moreover, PMF analysis showed that each of the six elements is mainly associated with a single factor, confirming that elemental distribution is homogenous. Taken together, the XRD, SEM/EDS, and PMF results indicate that the material can be classified as a HEO.

The HEOCs possess properties that makes them adequate for both the supply of lattice oxygen and the release of gaseous oxygen for CL processes. According to the experiments (TGA and BFBR), they display a reasonable reactivity compared with the rates of reaction for different benchmark OCs comprising of Cu, Fe and Mn. Furthermore, the chemical and physical characteristics of the materials make them suitable for

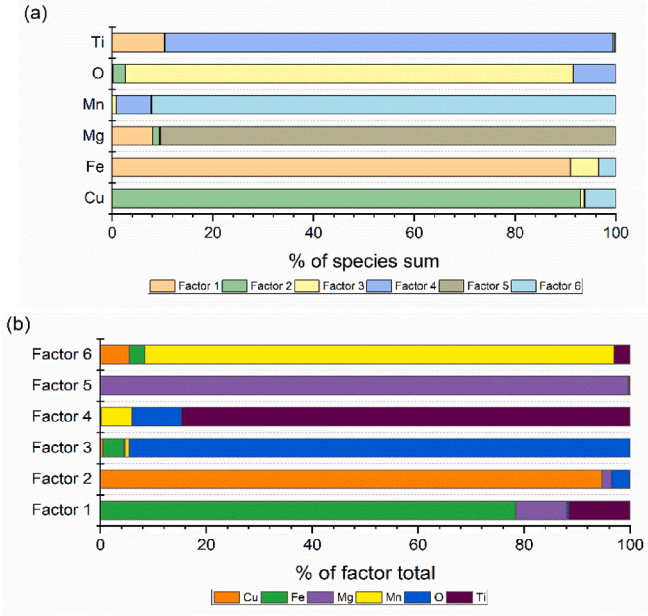

Fig. 6. (a) Species and (b) factor profiles from PMF analysis with a factor of six for used HEOC_1000.

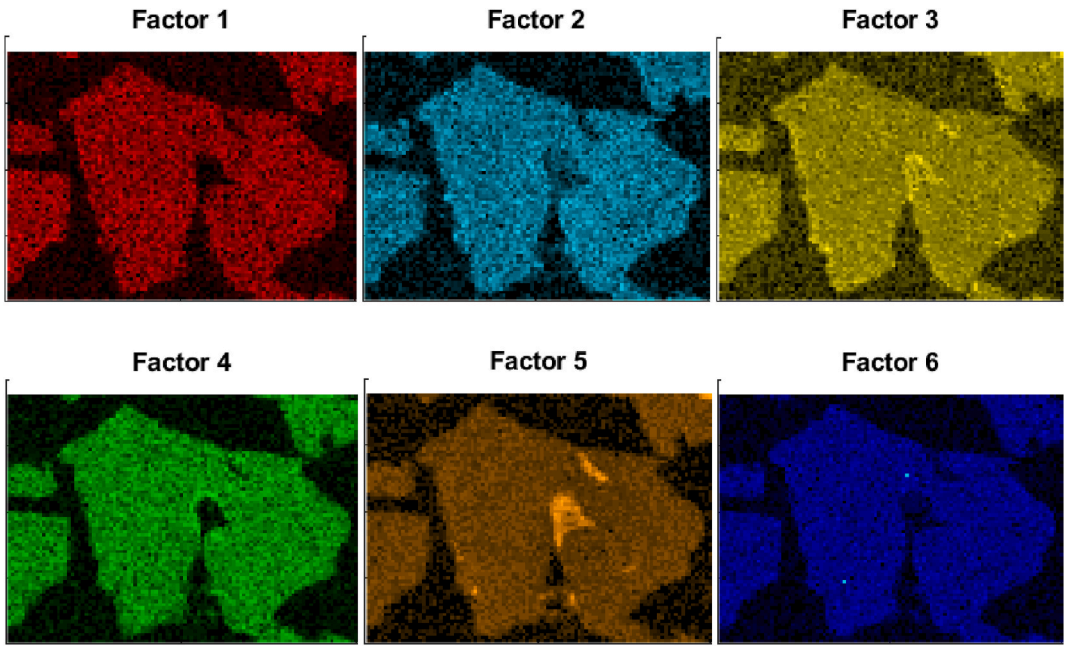

Fig. 7. Reconstruction of EDX images using the PMF factors.

use in fluidized beds. The current work, therefore, clearly demonstrates that the prepared HEOCs can be used in both CLC and CLOU processes.

CRediT authorship contribution statement

Iñaki Adánez-Rubio: Writing – review & editing, Writing – original draft, Visualization, Validation, Methodology, Investigation, Data curation, Conceptualization. **María T. Izquierdo:** Writing – review & editing, Writing – original draft, Data curation. **Joakim Brorsson:** Writing – review & editing, Writing – original draft. **Daofeng Mei:** Writing – review & editing, Writing – original draft, Validation, Data curation. **Tobias Mattisson:** Writing – review & editing, Validation, Supervision, Resources, Funding acquisition, Conceptualization. **Juan Adánez:** Writing – review & editing, Resources, Funding acquisition.

Declaration of competing interest

The authors declare that they have no known competing financial interests or personal relationships that could have appeared to influence the work reported in this paper.

Data availability

Data will be made available on request.

Acknowledgements

This work was partiatially funded by the Swedish Research Council (2020–03487) and the Gobierno de Aragón – Dpto. de Ciencia, Universidad y Sociedad del Conocimiento - Project LMP166_21. I. Adánez-Rubio acknowledges for “Juan de la Cierva” Program (Grant IJC2019-038987-I funded by MCIN/AEI/10.13039/501100011033) and for the “José Castillejo” international mobility program for young researchers (CAS21/00200).

Appendix A. Supplementary data

Supplementary data to this article can be found online at https://doi.org/10.1016/j.energy.2024.131307.

References

[1] Hossain MM, de Lasa HI. Chemical-looping combustion (CLC) for inherent CO_2 separations—a review. Chem Eng Sci 2008;63(18):4433–51.
[2] Adanez J, Abad A, Garcia-Labiano F, Gayan P, de Diego L. Progress in chemical-looping combustion and reforming technologies. Prog Energy Combust Sci 2012;38(2):215–82.
[3] Adánez J, Abad A, Mendiara T, Gayán P, de Diego LF, García-Labiano F. Chemical looping combustion of solid fuels. Prog Energy Combust Sci 2018;65:6–66.
[4] Curnan MT, Kitchin JR. Effects of concentration, crystal structure, magnetism, and electronic structure method on first-principles oxygen vacancy formation energy trends in perovskites. J Phys Chem C 2014;118(49):28776–90.
[5] Tabish A, Varghese AM, Wahab MA, Karanikolos GN. Perovskites in the energy grid and CO2 conversion: current context and future directions. Catalysts 2020;10(1).
[6] Tian M, Wang C, Han Y, Wang X. Recent advances of oxygen carriers for chemical looping reforming of methane. ChemCatChem 2021;13(7):1615–37.
[7] Qasim M, Ayoub M, Ghazali NA, Aqsha A, Ameen M. Recent advances and development of various oxygen carriers for the chemical looping combustion process: a review. Ind Eng Chem Res 2021;60(24):8621–41.
[8] Musicó BL, Gilbert D, Ward TZ, Page K, George E, Yan J, et al. The emergent field of high entropy oxides: design, prospects, challenges, and opportunities for tailoring material properties. Apl Mater 2020;8(4).
[9] Sun Y, Dai S. High-entropy materials for catalysis: a new frontier. Sci Adv 2021;7(20).
[10] Liu J, Li F. Mixed oxides as multi-functional reaction media for chemical looping catalysis. Chem Commun 2022;59(1):10–28.
[11] Sun Z, Russell CK, Whitty KJ, Eddings EG, Dai J, Zhang Y, et al. Chemical looping-based energy transformation via lattice oxygen modulated selective oxidation. Prog Energy Combust Sci 2023;96.
[12] Albedwawi SH, AlJaberi A, Haidemenopoulos GN, Polychronopoulou K. High entropy oxides-exploring a paradigm of promising catalysts: a review. Mater Des 2021;202.
[13] Batchelor TAA, Pedersen JK, Winther SH, Castelli IE, Jacobsen KW, Rossmeisl J. High-entropy alloys as a discovery platform for electrocatalysis. Joule 2019;3(3):834–45.
[14] Feng D, Dong Y, Zhang L, Ge X, Zhang W, Dai S, et al. Holey lamellar high-entropy oxide as an ultra-high-activity heterogeneous catalyst for solvent-free aerobic oxidation of benzyl alcohol. Angew Chem Int Ed 2020;59(44):19503–9.
[15] Riley C, de la Riva A, Park JE, Percival SJ, Benavidez A, Coker EN, et al. A high entropy oxide designed to catalyze CO oxidation without precious metals. ACS Appl Mater Interfaces 2021;13(7):8120–8.
[16] Pedersen JK, Batchelor TAA, Bagger A, Rossmeisl J. High-entropy alloys as catalysts for the CO_2 and CO reduction reactions. ACS Catal 2020;10(3):2169–76.
[17] Sarkar A, Wang Q, Schiele A, Chellali MR, Bhattacharya SS, Wang D, et al. High-entropy oxides: fundamental aspects and electrochemical properties. Adv Mater 2019;31(26).
[18] Lun Z, Ouyang B, Kwon DH, Ha Y, Foley EE, Huang TY, et al. Cation-disordered rocksalt-type high-entropy cathodes for Li-ion batteries. Nat Mater 2021;20(2):214–21.
[19] Sarkar A, Velasco L, Wang D, Wang Q, Talasila G, de Biasi L, et al. High entropy oxides for reversible energy storage. Nat Commun 2018;9(1).

[20] Fu M, Ma X, Zhao K, Li X, Su D. High-entropy materials for energy-related applications. iScience 2021;24(3).
[21] Zywczak A, Krawczyk PA, Jurczyszyn M, Pawlak J, Salamon W, Baran P, et al. High-entropy perovskites as multifunctional metal oxide semiconductors: synthesis and characterization of $(Gd_{0.2}Nd_{0.2}La_{0.2}Sm_{0.2}Y_{0.2})CoO_3$. ACS Appl Electron Mater 2020;2(10):3211–20.
[22] Aamlid SS, Oudah M, Rottler J, Hallas AM. Understanding the role of entropy in high entropy oxides. J Am Chem Soc 2023;145(11):5991–6006.
[23] Fu M, Ma X, Zhao K, Li X, Su D. High-entropy materials for energy-related applications. iScience 2021;24(3):102177.
[24] Li H, Sun Z, Cao Y. Particles attrition of binary mixtures in the coal-fueled chemical looping system based on fluidized bed. Particuology 2024;86:281–90.
[25] Kramp M, Thon A, Hartge EU, Heinrich S, Werther J. The role of attrition and solids recovery in a chemical looping combustion process. Oil Gas Sci Technol 2011;66 (2):277–90.
[26] Rydén M, Moldenhauer P, Lindqvist S, Mattisson T, Lyngfelt A. Measuring attrition resistance of oxygen carrier particles for chemical looping combustion with a customized jet cup. Powder Technol 2014;256:75–86.
[27] Scala F, Chirone R, Salatino P. Attrition phenomena relevant to fluidized bed combustion and gasification systems. Fluidized Bed Technologies for Near-Zero Emission Combustion and Gasification 2013:254–315.
[28] Cabello A, Gayán P, García-Labiano F, de Diego LF, Abad A, Adánez J. On the attrition evaluation of oxygen carriers in Chemical Looping Combustion. Fuel Process Technol 2016;148:188–97.
[29] Adánez-Rubio I, Abad A, Gayan P, de Diego LF, Adánez J. CLOU process performance with a Cu-Mn oxygen carrier in the combustion of different types of coal with CO_2 capture. Fuel 2018;212:605–12.
[30] Nelson T, van der Watt JG, Laudal D, Feilen H, Mann M, Srinivasachar S. Reactive jet and cyclonic attrition analysis of ilmenite in chemical looping combustion systems. Int J Greenh Gas Control 2019;91.
[31] Sun Y, Dai S. High-entropy materials for catalysis: a new frontier. Sci Adv 2021;7 (20):eabg1600.
[32] Albedwawi SH, AlJaberi A, Haidemenopoulos GN, Polychronopoulou K. High entropy oxides-exploring a paradigm of promising catalysts: a review. Mater Des 2021;202:109534.
[33] Zhong M, Xu T, Wang C, Teng Y, Cai Y, Zhang Z, et al. Utilizing high entropy oxide (Ni0.2Co0.2Ca0.2Cu0.2Mg0.2)Fe2O4 in chemical looping process for highly efficient and stable hydrogen production. Chem Eng J 2024;487:150521.
[34] Adánez-Rubio I, Pérez-Astray A, Mendiara T, Izquierdo MT, Abad A, Gayán P, et al. Chemical looping combustion of biomass: CLOU experiments with a Cu-Mn mixed oxide. Fuel Process Technol 2018;172:179–86.
[35] Adánez-Rubio I, Samprón I, Izquierdo MT, Abad A, Gayán P, Adánez J. Coal and biomass combustion with CO_2 capture by CLOU process using a magnetic Fe-Mn-supported CuO oxygen carrier. Fuel 2022;314.
[36] Johansson M, Mattisson T, Lyngfelt A. Investigation of Fe_2O_3 with $MgAl_2O_4$ for chemical-looping combustion. Ind Eng Chem Res 2004;43(22):6978–87.
[37] Paatero P, Tapper U. Positive matrix factorization: a non-negative factor model with optimal utilization of error estimates of data values. Environmetrics 1994;5 (2):111–26.
[38] Lee DD, Seung HS. Learning the parts of objects by non-negative matrix factorization. Nature 1999;401(6755):788–91.
[39] Kong X, Stanicic I, Andersson V, Mattisson T, Pettersson JBC. Phase recognition in SEM-EDX chemical maps using positive matrix factorization. MethodsX 2023;11: 102384.
[40] Norris G, Duvall R, Brown S, Bai S. EPA positive matrix factorization (PMF) 5.0 fundamentals and user guide. In: Development OoRa. US Environmental Protection Agency; 2014. Washington DC 20460.
[41] Adánez J, de Diego LF, García-Labiano F, Gayán P, Abad A, Palacios JM. Selection of oxygen carriers for chemical-looping combustion. Energy Fuels 2004;18(2): 371–7.
[42] Adánez-Rubio I, Arjmand M, Leion H, Gayán P, Abad A, Mattisson T, et al. Investigation of combined supports for Cu-based oxygen carriers for chemical-looping with oxygen uncoupling (CLOU). Energy Fuels 2013;27(7):3918–27.
[43] López-Vergara A, Porras-Vázquez JM, Infantes-Molina A, Canales-Vázquez J, Cabeza A, Losilla ER, et al. Effect of preparation conditions on the polymorphism and transport properties of $La_{6-x}MoO_{12-\delta}$ ($0 \leq x \leq 0.8$). Chem Mater 2017;29(16): 6966–75.
[44] Abad A, Gayán P, Mendiara T, Bueno JA, García-Labiano F, de Diego LF, et al. Assessment of the improvement of chemical looping combustion of coal by using a manganese ore as oxygen carrier. Fuel Process Technol 2018;176:107–18.
[45] Gayán P, Adánez-Rubio I, Abad A, de Diego LF, García Labiano F, Adánez J. Development of Cu-based oxygen carriers for chemical-looping with oxygen uncoupling (CLOU) process. Fuel 2012;96:226–38.
[46] Mendiara T, Pérez R, Abad A, De Diego LF, García-Labiano F, Gayán P, et al. Low-cost Fe-based oxygen carrier materials for the *i*G-CLC process with coal. 1. Ind Eng Chem Res 2012;51(50):16216–29.
[47] Rydén M, Leion H, Mattisson T, Lyngfelt A. Combined oxides as oxygen-carrier material for chemical-looping with oxygen uncoupling. Appl Energy 2014;113: 1924–32.
[48] Moldenhauer P, Hallberg P, Biermann M, Snijkers F, Albertsen K, Mattisson T, et al. Oxygen-carrier development of calcium manganite-based materials with perovskite structure for chemical-looping combustion of methane. Energy Technol 2020;8(6).
[49] Cabello A, Abad A, Gayán P, de Diego LF, García-Labiano F, Adánez J. Effect of operating conditions and H2S presence on the performance of CaMg0.1Mn0.9O3-δ perovskite material in chemical looping combustion (CLC). Energy Fuel 2014;28 (2):1262–74.
[50] Adánez-Rubio I, Filsouf A, Durmaz M, Mendiara T, Gayán P, Adánez J. Performance of a kaolin-doped, magnetic Cu-based oxygen carrier in biomass combustion. Powder Technol 2023;426:C7–118668.
[51] Cabello A, Abad A, Gayán P, García-Labiano F, de Diego LF, Adánez J. Increasing energy efficiency in chemical looping combustion of methane by in-situ activation of perovskite-based oxygen carriers. Appl Energy 2021;287.
[52] Fan Y, Siriwardane R, Tian H. Trimetallic oxygen carriers $CuFeMnO_4$, $CuFeMn_2O_4$, and $CuFe_{0.5}Mn_{1.5}O_4$ for chemical looping combustion. Energy Fuels 2015;29(10): 6616–24.
[53] Abad A, Mendiara T, Izquierdo MT, de Diego LF, García-Labiano F, Gayán P, et al. Evaluation of the redox capability of manganese-titanium mixed oxides for thermochemical energy storage and chemical looping processes. Fuel Process Technol 2021;211.
[54] Adánez-Rubio I, Abad A, Gayán P, Adánez I, De Diego LF, García-Labiano F, et al. Use of hopcalite-derived Cu-Mn mixed oxide as oxygen carrier for chemical looping with oxygen uncoupling process. Energy Fuels 2016;30(7):5953–63.
[55] Adánez-Rubio I, Izquierdo MT, Abad A, Gayan P, de Diego LF, Adánez J. Spray granulated Cu-Mn oxygen carrier for chemical looping with oxygen uncoupling (CLOU) process. Int J Greenh Gas Control 2017;65:76–85.
[56] Shulman A, Cleverstam E, Mattisson T, Lyngfelt A. Manganese/iron, manganese/nickel, and manganese/silicon oxides used in chemical-looping with oxygen uncoupling (CLOU) for combustion of methane. Energy Fuels 2009;23(10): 5269–75.
[57] Shulman A, Cleverstam E, Mattisson T, Lyngfelt A. Chemical – looping with oxygen uncoupling using Mn/Mg-based oxygen carriers – oxygen release and reactivity with methane. Fuel 2011;90(3):941–50.
[58] Mattisson T, Jing D, Lyngfelt A, Rydén M. Experimental investigation of binary and ternary combined manganese oxides for chemical-looping with oxygen uncoupling (CLOU). Fuel 2016;164:228–36.
[59] Rydén M, Leion H, Mattisson T, Lyngfelt A. Combined oxides as oxygen-carrier material for chemical-looping with oxygen uncoupling. Appl Energy 2014;113: 1924–32.
[60] Johnsson M, Lemmens P. Crystallography and chemistry of perovskites. Handbook of Magnetism and Advanced Magnetic Materials 2007.